MEMBRANES

Wrinkled metal-organic framework thin films with tunable Turing patterns for pliable integration

Xinyu Luo[1,2], Ming Zhang[1,2], Yubin Hu[1,2], Yan Xu[3], Haofei Zhou[3], Zijian Xu[4,5,6], Yinxuan Hao[3], Sheng Chen[4,5,6], Shengfu Chen[1], Yingwu Luo[1], Yiliang Lin[7], Junjie Zhao[1,2]*

Flexible integration spurs diverse applications in metal-organic frameworks (MOFs). However, current configurations suffer from the trade-off between MOF loadings and mechanical compliance. We report a wrinkled configuration of MOF thin films. We established an interfacial synthesis confined and controlled by a polymer topcoat and achieved multiple Turing motifs in the wrinkled thin films. These films have complete MOF surface coverage and exhibit strain tolerance up to 53.2%. The enhanced mechanical properties allow film transfer onto various substrates. We obtained membranes with large H_2/CO_2 selectivity (41.2) and high H_2 permeance (8.46×10^3 gas permeation units), showcasing negligible defects after transfer. We also achieved soft humidity sensors on delicate electrodes by avoiding exposure to harsh MOF synthesis conditions. These results highlight the potential of wrinkled MOF thin films for plug-and-play integration.

Unlocking the full potential of metal-organic frameworks (MOFs) necessitates integration with maximal exposed active surfaces. This is essential for applications as diverse as membranes, electronics, and biomedical devices (1–6). However, a fundamental trade-off exists: Increasing the MOF mass fraction on the surface inevitably compromises the mechanical properties, resulting in stiffer and more brittle materials. Prior attempts to navigate this challenge, specifically in thin film configurations (7–9), have faced limitations because of the inherently low fracture strain of MOFs (10). These configurations are especially vulnerable when paired with deformable substrates, often leading to cracks and failures under insubstantial strain.

We report a wrinkled configuration for MOF thin films (Fig. 1A). The deformable structures confer enhanced strain tolerance, and the wrinkles provide additional exposed surfaces compared with that of planar configurations. Unlike common methods to produce wrinkled structures in other inorganic materials (11–14), we developed a synthesis protocol that uses diffusion-driven instability to generate wrinkled MOF thin films. Predicted by Alan Turing (15), a pronounced difference in the diffusion rates of two reagents may induce instability that leads to local activation and long-range inhibition (16, 17). The resulting spatiotemporal distribution of the product concentration is desired for the generation of a wrinkled surface. In our synthesis, we used a polymer topcoat (PEBAX-2533; a block copolymer with soft polyether blocks and rigid polyamide blocks) to provide a confined venue for the interfacial reaction on an atomic layer deposited (ALD) ZnO sur-

[1]State Key Laboratory of Chemical Engineering, College of Chemical and Biological Engineering, Zhejiang University, Hangzhou, Zhejiang 310027, China. [2]Institute of Zhejiang University–Quzhou, Quzhou, Zhejiang 324000, China. [3]School of Aeronautics and Astronautics, Zhejiang University, Hangzhou, Zhejiang 310027, China. [4]Shanghai Synchrotron Radiation Facility, Shanghai Advanced Research Institute, Chinese Academy of Sciences, Shanghai 201204, China. [5]Shanghai Institute of Applied Physics, Chinese Academy of Sciences, Shanghai 201800, China. [6]University of Chinese Academy of Sciences, Beijing 100049, China. [7]Department of Chemical and Biomolecular Engineering, National University of Singapore, 117585, Singapore.
*Corresponding author. Email: junjiezhao@zju.edu.cn

Fig. 1. Wrinkled configuration of MOF thin films with Turing patterns to enable plug-and-play integration. (**A**) Compared with planar films and mixed matrix configurations, the proposed wrinkled film structure is deformable and transferable while maintaining high surface MOF fraction. (**B**) Schematic of the confined interfacial synthesis for wrinkled MOF films. Local activation through rapid HKUST-1 formation and lateral inhibition by the as-formed MOF led to the generation of Turing patterns. (**C** and **D**) Envisioned plug-and-play integration for the wrinkled MOF films. By transferring MOF Turing films onto porous supports and IDEs on flexible substrates, (C) gas separation membranes and (D) soft sensors were achieved.
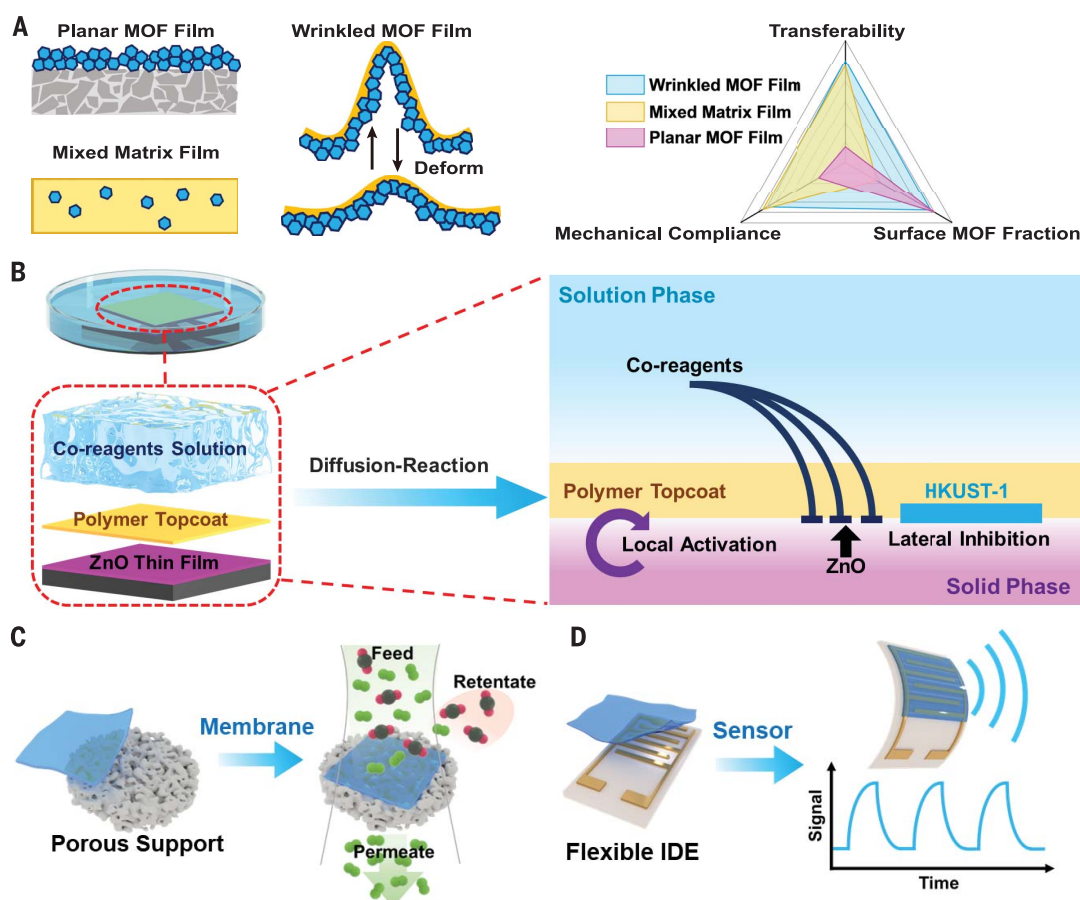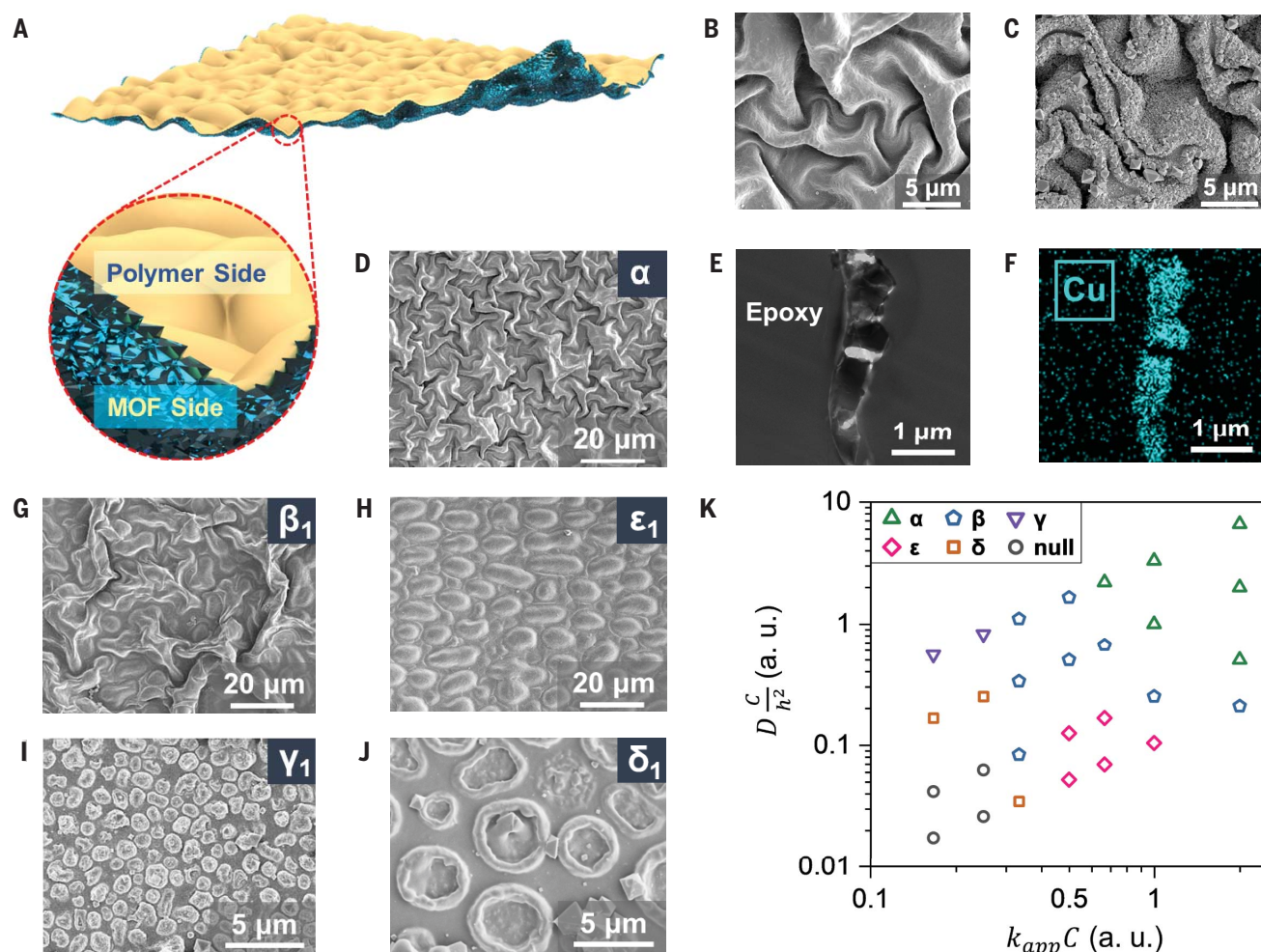
Fig. 2. Tuning synthesis conditions for various MOF Turing patterns.
(**A**) Illustration of the Janus structure in the wrinkled MOF films. (**B** and **C**) SEM images of the labyrinthine Turing structures on the (B) top and (C) bottom surfaces of the wrinkled thin film. (**E**) Cross-sectional TEM and (**F**) EDX mapping images for the Janus film structure with HKUST-1 Turing patterns. (**D** and **G** to **J**) SEM images of five representative categories of Turing patterned films. (**K**) Experimental map specifying the reaction ($k_{app}C$) and diffusion ($D\frac{C}{h^2}$) conditions for different types of MOF Turing patterns.

face while controlling the diffusion of the MOF co-reagents [Cu(NO$_3$)$_2$ and trimesic acid] toward the polymer-ZnO interface (Fig. 1B and figs. S1 to S3). Within this confined space, the basic hydrolysis product released from the ZnO surface diffused upward (figs. S4 and S5) and initiated rapid HKUST-1 [Cu$_3$(BTC)$_2$, where BTC is benzene-1,3,5-tricarboxylate] formation upon exposure to the co-reagents (18, 19), providing the essential short-range activation. The as-formed MOF nuclei and nanoparticles obstructed the diffusion of the reactants, fulfilling the inhibition requisite for Turing patterns. Our mathematical modeling predicted that tuning the reagent concentration and the thickness of the polymer topcoat is effective to change the reaction-diffusion conditions for achieving multiple types of Turing patterns (figs. S6 and S7). Accordingly, we experimentally explored these two parameters and achieved wrinkled MOF thin films with tunable Turing motifs. Such wrinkled MOF films can be easily transferred

onto various substrates for applications such as gas separation membranes (Fig. 1C) and soft sensors (Fig. 1D).

A wrinkled MOF film fabricated on a 10.16-cm wafer is shown in fig. S8. This wrinkled film exhibits a Janus structure (Fig. 2A): The bottom side exposes a continuous layer of HKUST-1 (Fig. 2C), whereas the top side exhibits negligible presence of MOF crystals (Fig. 2B). The labyrinthine stripes observed on this film with both scanning electron microscopy (SEM) (Fig. 2, B and C) and optical microscopy (fig. S9) correspond to a classical type of Turing pattern (20, 21). X-ray diffraction and Fourier-transform infrared spectroscopy (figs. S10 and S11) confirmed that the wrinkled crystalline thin film is composed of HKUST-1. Transmission electron microscopy (TEM) and energy dispersive x-ray (EDX) mapping images (Fig. 2, E and F, and fig. S12) further reveal that the ultrathin polymer skin layer maintains the integrity of the wrinkled MOF thin film.

Ptychographic tomography further shows the three-dimensional (3D) structure of the MOF wrinkles (fig. S13). Thermogravimetric analysis (fig. S14) reveals that the MOF loading reached at least 96.3 wt %, which is greater than that of previously reported MOF-based hybrid materials and composites (22–27). Such a high MOF fraction ensures that the Brunauer-Emmett-Teller (BET) surface area of the MOF Turing film (1473 m^2 g^{-1}) reaches close alignment with bulk HKUST-1 (fig. S15).

This confined interfacial synthesis system offers a high degree of control and versatility, allowing for the generation of diverse Turing patterns. By tuning the topcoat thickness (h) (table S1) and the co-reagent concentration (C) at a fixed temperature of 298.15 K, we obtained 13 distinct Turing patterns (Fig. 2, D and G to J, and figs. S16 to S23) that can be grouped into five motif-based categories. To present our findings more clearly, we used $k_{app}C$ to represent the reaction rate (k_{app} is defined as the apparent
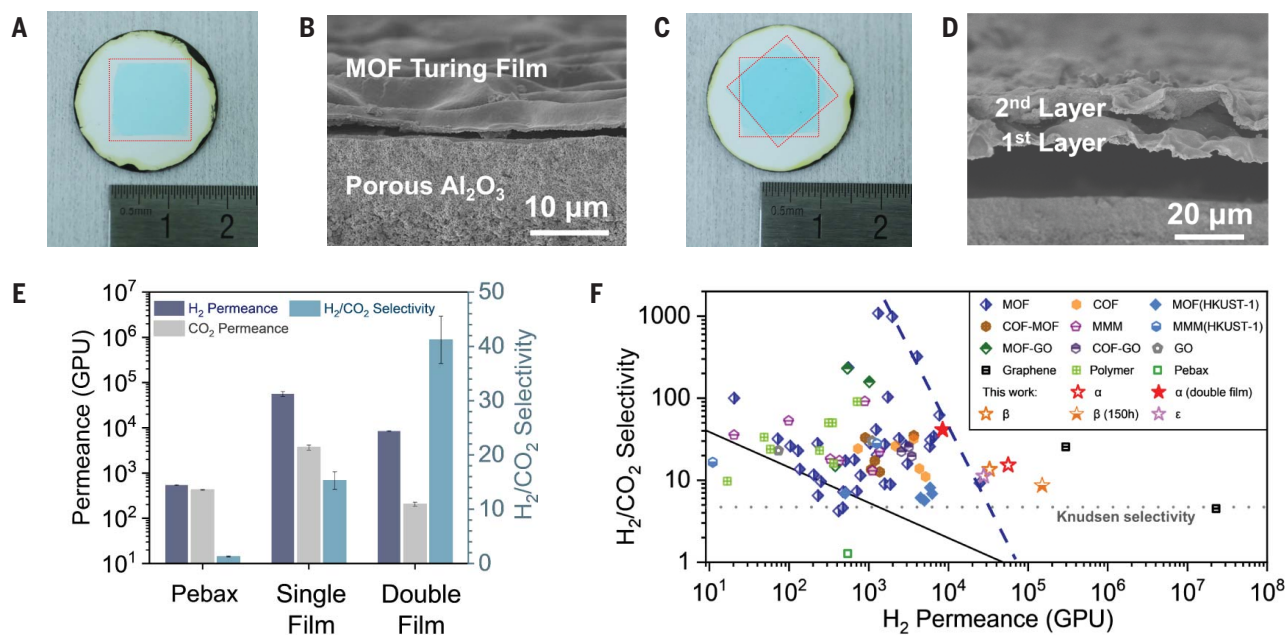
Fig. 3. MOF Turing film transferred onto porous alumina support for gas separation membrane. (**A**) Photograph and (**B**) cross-sectional SEM image of the membrane structure with single film transfer. (**C**) Photograph and (**D**) cross-sectional SEM image of the stacked Turing films obtained after transfer twice. The red dashed rectangles in (A) and (C) outline the position of the MOF Turing films after transfer. (**E**) H_2/CO_2 separation performance for the MOF Turing films supported on porous alumina and spin-coated Pebax-2533 film (~100 nm) on porous alumina. Error bars indicate SDs. (**F**) Comparison of the H_2/CO_2 separation performances of our membranes with other state-of-art membranes. The Robeson's upper bound (2008) was plotted as the solid black line by assuming the membrane thickness of 0.1 μm when converting the permeability into permeance. The blue dashed line indicates the current permeance upper bound of MOF-containing membranes (tables S3 and S4). COF, covalent organic framework; MMM, mixed matrix membrane; GO, graphene oxide.

kinetic constant) under the assumption of pseudo-first-order kinetics and used $D\frac{C}{h^2}$ as the effective diffusion rate (where D is the co-reagent diffusivity). This led us to create an experimental map (Fig. 2K) that illustrates the regions of conditions where specific patterns emerge, which highly resembles the condition map obtained from our modeling (fig. S24).

Indicated with the green triangles in Fig. 2K, high reaction and diffusion rates led to formation of group α patterns, which comprises labyrinthine structures (Fig. 2D) commonly found in Turing patterns (20, 21, 28). In comparison, the gray circles on the other end of Fig. 2K indicate conditions of low reaction and diffusion rates, which forbid the generation of any Turing pattern.

The blue pentagons in Fig. 2K indicate the conditions that yielded group β patterns featuring superposed motifs. With relatively high $k_{app}C$, flake-like spots with dimensions of ~5 μm were found intersecting with labyrinthine stripes ($β_1$) (Fig. 2G). In conditions of moderate $k_{app}C$, circular areas filled with small dots (~1 μm in size) appeared amid the $β_1$-like features ($β_2$) (fig. S17), which are similar to the superposition patterns theoretically predicted in earlier work (29). With relatively low $k_{app}C$, wrinkle-enclosed craters surrounded by densely packed $β_1$-like spots were achieved ($β_3$) (fig. S18), which resemble the skin of a moray eel (30).

Groups γ and δ were formed in the regime of low $k_{app}C$ values. The purple triangles in Fig. 2K indicate group γ, which is characterized by dot motifs (Fig. 2I) that vary in density and size (fig. S19). Group δ patterns, indicated in Fig. 2K with orange squares, display O-shape (Fig. 2J) and C-shape (fig. S20) motifs reminiscent of leopard skin (30) and share similarities with the simulated patterns reported by Kondo and Miura (16).

The pink rhombuses in Fig. 2K indicate the conditions for generating group ε patterns, particularly when small $D\frac{C}{h^2}$ values are present. These patterns predominantly include oval motifs ($ε_1$) (Fig. 2H) that can either evolve into worm-like forms ($ε_2$) or partially transform into irregular dapples ($ε_3$) (15) because of slight changes in C and h (figs. S21 and S22).

Facile transferability for membrane fabrication

We sought to explore the potential applications of these structures beyond their native substrate. Because of the consumption of ZnO in the confined interfacial synthesis, the as-formed films can be detached from the Si substrate and placed onto new surfaces (fig. S25). Such transferability combined with the strain tolerance enables plug-and-play integration of MOF thin films with diverse substrates.

We transferred our wrinkled MOF thin films with Turing patterns onto porous alumina sup-ports to create membranes (Fig. 3, A and B). Subsequent SEM revealed no cracks or defects, confirming the structural integrity of the films after transfer (fig. S26). Additionally, we used small gas molecules as probes to evaluate the film quality. We assessed with the Wicke-Kallenbach method the membrane separation performance for equimolar binary mixtures of H_2/CO_2 (fig. S27). With a single film transfer (Fig. 3A), the H_2/CO_2 selectivity (15.3) was found well above the Knudsen selectivity (4.69), indicating negligible pinhole defects. The corresponding H_2 permeance reaches up to 6.82×10^4 gas permeation units (GPU; 1 GPU = 3.35×10^{-10} mol s^{-1} m^{-2} Pa^{-1}) (table S2), which is greater than previously reported MOF-containing membranes (Fig. 3F) (31–35). The small thickness of our wrinkled MOF surface leads to the low permeation resistance. In addition, the increased effective surface area by the wrinkled structures contributes to the enhanced H_2 permeance. As the ratio of the effective membrane area to the projected area increased from 2.5 (type ε) to 4.2 (type α) (fig. S28), the H_2 permeance rose from $(2.77 \pm 0.22) \times 10^4$ GPU (type ε) to $(5.62 \pm 0.68) \times 10^4$ GPU (type α). We used the solution-diffusion model (36) and confirmed a diffusion-driven separation mechanism (fig. S29) (37).

We layered one MOF Turing film atop another, creating stacked film structures on porous
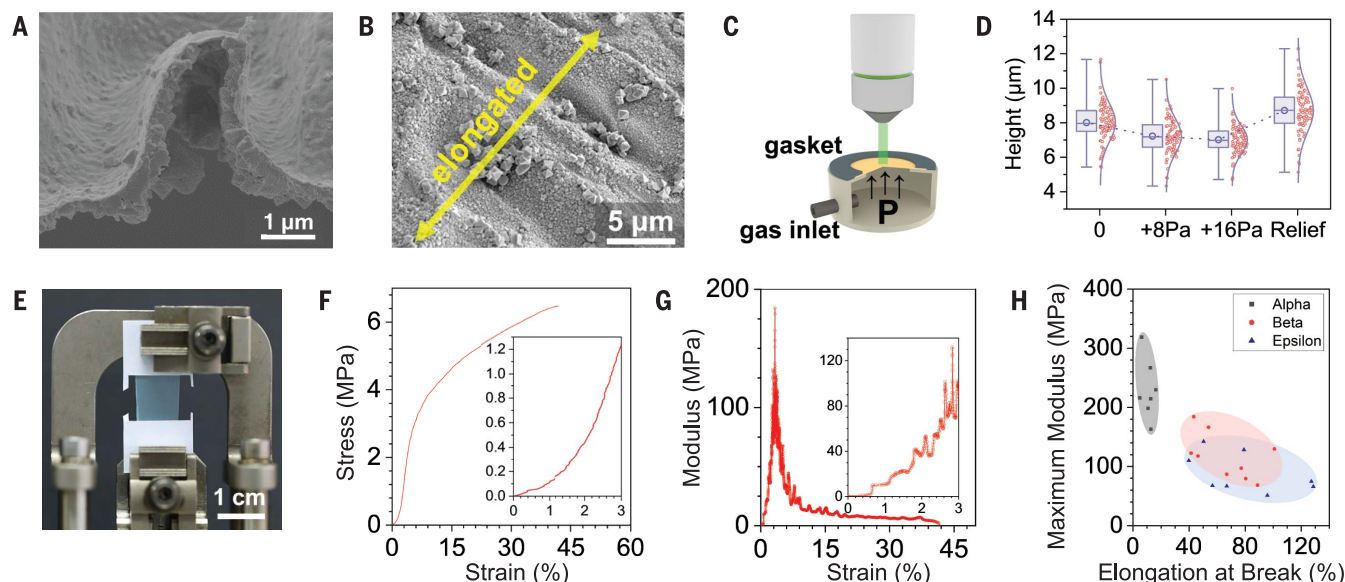
Fig. 4. Stretchable MOF Turing film for soft integrations. (**A** and **B**) SEM images of the wrinkles in the MOF Turing film (A) before and (B) after uniaxial elongation. (**C**) Schematic of the customized cell built for in situ measurement of film expansion. (**D**) Box plot for the distribution of heights of wrinkles during film expansion and relief. Whiskers are defined to cover 100% of the data. Center lines indicate the medians. Box limits indicate the 25th and 75th percentiles. Blue open circles indicate the means. (**E**) Photo of MOF Turing film during uniaxial tensile testing. (**F**) Stress-strain curve obtained for a wrinkled MOF film with type β Turing patterns. (Inset) The change of stress in the initial strain. (**G**) Modulus calculated from the stress-strain curve in Fig. 4F. (Inset) The change of modulus in the initial strain. (**H**) Maximum modulus and elongation at break of the winkled MOF thin films with different types of Turing motifs measured with uniaxial tensile tests.

alumina (Fig. 3, C and D). Such configuration enabled enhanced H_2/CO_2 selectivity up to 41.2 (Fig. 3E) while sustaining H_2 permeance at 8.46×10^3 GPU. Both single- and double-film configurations surpass the Robeson upper bound (Fig. 3F) (38). We also evaluated the long-term performance of our MOF Turing film and found that the single layer of type β Turing film reached a H_2 permeance of 1.5×10^5 GPU while maintaining a H_2/CO_2 selectivity of 8.6 after 150 hours of testing.

Strain tolerance for flexible integration

Beyond integration with rigid surfaces, our MOF Turing films also exhibit stretchability, potentially expanding their compatibility with soft substrates. The hinge-like structures in our film (Fig. 4A) were observed to deform under uniaxial elongation (Fig. 4B) similar to prior wrinkled films of other inorganic materials (13), enabling strain as large as 29.5%. Whereas most MOF-containing film structures have brittle properties (39), no cracks were found in our elongated film (fig. S30). To delve deeper into the mechanical robustness of our MOF Turing films, we custom built a pressurized cell for in situ film expansion measurements by means of 3D optical profilometry (Fig. 4C). We fixed and sealed a piece of MOF Turing film over the cell's circular aperture and gradually increased the internal pressure by pumping air inside. As the pressure escalated, we observed a narrowing in the distribution of wrinkle heights (Fig. 4D). Our films

were found to withstand a maximum strain of 53.2% (figs. S31 and S32). Although no previous data are available for direct comparison with planar MOF thin films, the intrinsic limit of bulk MOFs was reported below 0.3% (40, 41). Upon pressure release, the distribution of wrinkle heights returned to a state similar to the initial configuration, substantiating the mechanical resilience of our films.

We performed uniaxial tensile tests to investigate how Turing structures affect the mechanical properties. We show in Fig. 4E a wrinkled MOF thin film with type β Turing pattern under tensile testing by means of a dynamic mechanical analyzer (DMA) (fig. S33). The corresponding stress-strain curve (Fig. 4F) reveals an elongation at break of 41.6%. A strain-hardening behavior was found similar to that of other wrinkled structures (42). The modulus calculated from the stress-strain curve exhibits oscillatory changes with the strain (Fig. 4G), showing the stress dissipation by the wrinkled structures. In Fig. 4H, we compare the mechanical properties of the MOF Turing films with different patterns. Type α tends to show a higher maximum modulus but smaller elongation at break than that of the other two Turing patterns. This result suggests that the line structures of type β and the ellipsoidal surface of type ε may allow easier elastic deformation than that of type α in the uniaxial tensile tests.

The mechanical properties of our MOF Turing films enable the integration with delicate substrates for soft electronics. A notable demand

lies in interdigitated electrodes (IDEs) on polymer substrates, which are often used in flexible sensors. However, these IDEs are vulnerable to solvent-induced damage in the solvothermal environment typical for MOF thin film growth. Using a transfer method akin to the above-mentioned membrane fabrication, we successfully aligned and attached our MOF Turing film to the active IDE area, with the MOF side facing the air (fig. S34). The resulting sensor device is bendable to conform to curved surfaces such as the external wall of a scintillation vial (fig. S34). To gauge the sensing performance, we monitored the capacitive response to diluted water vapor at room temperature (fig. S35). Both planar and bent configurations exhibit a consistent linear response for concentrations spanning from 300 to 1000 parts per million (ppm) (fig. S36A). Furthermore, we observed repetitive responses upon successive water vapor exposures (fig. S36B). In addition to HKUST-1, we also demonstrated that our synthesis can be applied to ZIF-65-I, and we achieved type δ Turing patterns in the thin film (figs. S37 and S38). These results underscore the promise of our wrinkled MOF thin film for plug-and-play integration, with a range of substrates and potential applications.

REFERENCES AND NOTES

1. S. J. Datta et al., Science **376**, 1080–1087 (2022).
2. Z. Yang, D. Zhao, Science **381**, 1288–1289 (2023).
3. M. Orfano et al., Nat. Photonics **17**, 672–678 (2023).
4. K. Ni et al., Nat. Biomed. Eng. **6**, 144–156 (2022).
5. I. Stassen et al., Chem. Soc. Rev. **46**, 3185–3241 (2017).

6. O. Shekhah et al., Chem. Commun. 50, 2089–2092 (2014).
7. M. S. Denny Jr., J. C. Moreton, L. Benz, S. M. Cohen, Nat. Rev. Mater. 1, 16078 (2016).
8. M. Kalaj et al., Chem. Rev. 120, 8267–8302 (2020).
9. Q. Qian et al., Chem. Rev. 120, 8161–8266 (2020).
10. N. C. Burtch, J. Heinen, T. D. Bennett, D. Dubbeldam, M. D. Allendorf, Adv. Mater. 30, e1704124 (2018).
11. N. Bowden, S. Brittain, A. G. Evans, J. W. Hutchinson, G. M. Whitesides, Nature 393, 146–149 (1998).
12. G. Dong et al., Adv. Mater. 32, e2004477 (2020).
13. J. A. Rogers, T. Someya, Y. Huang, Science 327, 1603–1607 (2010).
14. D.-Y. Khang, H. Jiang, Y. Huang, J. A. Rogers, Science 311, 208–212 (2006).
15. A. M. Turing, Philos. Trans. R. Soc. Lond. B Biol. Sci. 237, 37–72 (1952).
16. S. Kondo, T. Miura, Science 329, 1616–1620 (2010).
17. A. Gierer, H. Meinhardt, Kybernetik 12, 30–39 (1972).
18. J. Zhao et al., J. Am. Chem. Soc. 137, 13756–13759 (2015).
19. J. Zhao, B. Kalanyan, H. F. Barton, B. A. Sperling, G. N. Parsons, Chem. Mater. 29, 8804–8810 (2017).
20. J. E. Pearson, Science 261, 189–192 (1993).
21. Z. Tan, S. Chen, X. Peng, L. Zhang, C. Gao, Science 360, 518–521 (2018).
22. J. Zhao et al., Adv. Mater. Interfaces 1, 1400040 (2014).
23. Y. Zhang, Y. Zhang, X. Wang, J. Yu, B. Ding, ACS Appl. Mater. Interfaces 10, 34802–34810 (2018).
24. D. B. Dwyer et al., ACS Appl. Mater. Interfaces 10, 25794–25803 (2018).
25. Y. Zhang et al., J. Am. Chem. Soc. 138, 5785–5788 (2016).
26. J. C. Moreton, M. S. Denny, S. M. Cohen, Chem. Commun. 52, 14376–14379 (2016).
27. H. Wang et al., Nat. Commun. 10, 4204 (2019).
28. K. J. Lee, W. D. McCormick, Q. Ouyang, H. L. Swinney, Science 261, 192–194 (1993).
29. L. Yang, M. Dolnik, A. M. Zhabotinsky, I. R. Epstein, Phys. Rev. Lett. 88, 208303 (2002).
30. M. Malheiros, M. Walter, in Proceedings of the 43rd Graphics Interface Conference (Canadian Human-Computer Communications Society, 2017), pp. 148–155.
31. Y. Qin, L. Xu, L. Liu, Z. Ding, Ind. Eng. Chem. Res. 60, 1387–1395 (2021).
32. K. Yang et al., J. Membr. Sci. 611, 118419 (2020).
33. K. Yang et al., Sci. Bull. 66, 1869–1876 (2021).
34. H. Song et al., Angew. Chem. Int. Ed. 62, e202218472 (2023).
35. L. Shu et al., Angew. Chem. Int. Ed. 61, e202117577 (2022).
36. J. G. Wijmans, R. W. Baker, J. Membr. Sci. 107, 1–21 (1995).
37. H. Guo, G. Zhu, I. J. Hewitt, S. Qiu, J. Am. Chem. Soc. 131, 1646–1647 (2009).
38. L. M. Robeson, J. Membr. Sci. 320, 390–400 (2008).
39. Y. Zhao et al., J. Am. Chem. Soc. 142, 20915–20919 (2020).
40. T. To et al., Nat. Commun. 11, 2593 (2020).
41. M. Tricarico, C. Besnard, G. Cinque, A. M. Korsunsky, J.-C. Tan, Commun. Mater. 4, 86 (2023).
42. A. Sarafraz et al., J. Appl. Phys. 130, 184302 (2021).

SUPPLEMENTARY MATERIALS

science.org/doi/10.1126/science.adn8168
Materials and Methods
Supplementary Text
Figs. S1 to S38
Tables S1 to S4
References (43–123)